AIAA JOURNAL
Vol. 37, No. 3, March 1999

Finite Volume Algorithm to Compute Dense Compressible Gas–Solid Flows

Laure Combe* and Jean-Marc Hérard†
Electricité de France, 78400 Chatou, France

A finite volume scheme is presented that allows the performance of numerical simulations of a four-equation compressible two-fluid model on unstructured meshes. The convective part of the whole set of governing equations is a nonconservative conditionally hyperbolic system. To solve the latter, a fractional step method is presented, which is based on a splitting of convective fluxes. Approximate Roe-type Riemann solvers are used to compute numerical convective fluxes. Some computations of shock-tube test cases are presented and compared with numerical results of a three-equation model, which assumes equal velocities within each phase. A steady computation of a gas–solid flow in a simple nozzle is described, and an unsteady computation of a dense fluidized bed is also presented. Particular emphasis is given to the preservation of the maximum principle for the volumetric fraction.

I. Introduction

THE recent increase in computational facilities has favored the development of new physical models as well as new numerical techniques to predict gas–solid two-phase flows, using the two-fluid approach. Clearly the range of industrial applications is wide. It is well known that accurate computations require developing suitable algorithms. Some approximate Riemann solvers have been recently proposed to cope with two-fluid computations of compressible flows within the frame of dilute regimes.[1–5] Among the proposed solvers some try to inherit the stability of Roe's approximate Riemann solver, using a so-called weak formulation of the latter scheme. Others are based on Godunov's scheme for gasdynamics. In the present contribution, a way to extend these methods to the frame of dense situations, where both the volumetric fraction of the solid phase and the relative velocities may become great, is proposed.

In many industrial situations, the motion of a compressible gas–solid mixture in thermal equilibrium may be described by a four-equation model[2,6,7] including mass conservation of both phases and momentum equations for both the gas and the solid phase (see Refs. 8 and 9 for a two-fluid approach with help of a six-equation model). Despite its apparent simplicity, this continuous model intrinsically contains many difficulties. First, the convective subset has no conservative form; second, the latter convective subset is not an unconditional hyperbolic system; eventually, many different timescales are involved in this system. The algorithm to be detailed aims at overcoming the mentioned troubles.

The set of partial differential equations is presented in the next section. In Sec. III, an entropy characterization is exhibited, and hyperbolicity criteria associated with the nonconservative convective subset are given. The entropy inequality is useful to check the suitability of computational results. As with most currently known two-fluid models, the overall solution of the one-dimensional Riemann problem associated with the whole convective system cannot be solved for arbitrary initial data. Consequently, no exact or even approximate Riemann solver may be exhibited to solve the latter system. The finite volume algorithm, which is presented in the following section, takes advantage of the fractional step method to preserve the maximum principle for the volumetric fraction. Both the solution of one-dimensional Riemann problems involved within each step and associated approximate Riemann solvers are detailed. The analysis of a nonconservative Riemann problem requires application of recent theoretical results.[2,10–12] Some numerical results obtained on unstructured meshes are presented that confirm the robustness of the whole algorithm. Emphasis is given to test cases involving very high values of the volumetric fraction, which occur, e.g., when dense fluidized beds are computed, or when one attempts to simulate impinging jets highly loaded with particles.

II. Equations Set

Subscripts for the gas phase and the particle phase are 1 and 2, respectively. The volumetric fraction of solid particles is α_2, and its counterpart for the gas phase is $\alpha_1 = 1 - \alpha_2$, where α_2 is assumed to lie in [0, 1]. The positive density of the gas is ρ_1, and the constant density of particles is ρ_2; only heavy particles are considered herein and, thus, added mass effects are neglected. U^i is the velocity within phase i, and I_1 is the interfacial momentum transfer term, which accounts for drag effects only. The governing equations are

$$(\alpha_1\rho_1)_{,t} + \nabla\cdot\left(\alpha_1\rho_1\boldsymbol{U}^1\right) = 0 \tag{1}$$

$$(\alpha_2)_{,t} + \nabla\cdot\left(\alpha_2\boldsymbol{U}^2\right) = 0 \tag{2}$$

$$\left(\alpha_1\rho_1\boldsymbol{U}^1\right)_{,t} + \nabla\cdot\left(\alpha_1\rho_1\boldsymbol{U}^1\otimes\boldsymbol{U}^1\right) = -\alpha_1\nabla P_1(\rho_1) + \alpha_1\rho_1 g + I_1 - \nabla\cdot\left(\alpha_1\sum_1^{\text{visc}}\right) \tag{3}$$

$$\left(\alpha_2\rho_2\boldsymbol{U}^2\right)_{,t} + \nabla\cdot\left(\alpha_2\rho_2\boldsymbol{U}^2\otimes U^2\right) = -\alpha_2\nabla P_1(\rho_1) + \alpha_2\rho_2 g - \nabla\Xi(\alpha_2) - I_1 - \nabla\cdot\left(\alpha_2\sum_2^{\text{visc}}\right) \tag{4}$$

where $P_1(\rho_1)$ is the mean pressure within the gas phase

$$P_1(\rho_1) = \kappa\rho_1^{\gamma} \tag{5}$$

and $\Xi(\alpha 2)$ is the intergranular pressure

$$\Xi(\alpha_2) = \tfrac{2}{3}\rho_2\left(q_2^2\right)_0\alpha_2^{\frac{5}{3}}g(\alpha_2) \tag{6}$$

and where g is a monotone increasing function of the volumetric fraction

$$g(\alpha_2) = \left\{1 + \frac{2(1+e_c)\alpha_2}{\left[1-\left(\alpha_2/\alpha^{\max}\right)\right]^{\frac{5}{2}\alpha^{\max}}}\right\} \times \exp\left\{\frac{4\alpha^{\max}(1+e_c)}{[(15/2)\alpha^{\max}-3]}\left(1-\frac{\alpha_2}{\alpha^{\max}}\right)^{1-\frac{5}{2}\alpha^{\max}}\right\} \tag{7}$$

Received May 28, 1997; presented as Paper 97-2082 at the AIAA 13th Computational Fluid Dynamics Conference, Snowmass Village, CO, June 29–July 2, 1997; revision received Sept. 19, 1998; accepted for publication Oct. 27, 1998.

*Ph.D. Student, Direction des Etudes et Recherches, Département Laboratoire National d'Hydraulique, 6 quai Watier; also Ph.D. Student, Institut de Mécanique des Fluides de Toulouse, Avenue du Professor Camille Soula, 31400 Toulouse, France.

†Research Scientist, Direction des Etudes et Recherches, Département Laboratoire National d'Hydraulique, 6 quai Watier. Member AIAA.

In Eq. (7), $\alpha^{\max}$ is the maximum compactness rate and e_c the elasticity coefficient. In practice, we will set $\alpha^{\max} = 0.64$ and $e_c = 1$. The equation of state (7) results from integration of the particle energy governing equation, assuming a vacuum of gas and focusing on regular solutions (see Appendix 1 in Ref. 13, which is based on recent contributions[6–8,14]). As pointed out by the authors of Refs. 13 and 15 and briefly recalled subsequently, the asymptotic behavior in the vicinity of $\alpha^{\max}$ is crucial to ensure that the maximum principle for the volumetric fraction is preserved. Viscous contributions take the following form:

$$\sum_{1}^{\text{visc}} = -\mu_1 \left\{ \nabla(U^1) + \nabla^t(U^1) - \frac{2}{3}\nabla \cdot (U^1) I \right\} \tag{8a}$$

$$\sum_{2}^{\text{visc}} = -\mu_2 \left\{ \nabla(U^2) + \nabla^t(U^2) - \frac{2}{3}\nabla \cdot (U^2) I \right\} \tag{8b}$$

Drag effects are accounted for through

$$I_1 = K\alpha_1\alpha_2\rho_1(\boldsymbol{U}^2 - \boldsymbol{U}^1) \tag{9}$$

The positive drag coefficient K is in agreement with forms detailed in Refs. 7 and 8 and, thus, is not recalled herein; this means that for dilute regimes, the single-sphere drag formula is used and that Ergun's relation is considered for dense regions.

III. Some Basic Results

When viscous effects are neglected, discontinuous solutions may develop; an entropy inequality is, thus, essential to select physical solutions. For that purpose, we introduce the conservative variable

$$W^t = \left(\alpha_1\rho_1, \alpha_2, \alpha_1\rho_1 U_x^1, \alpha_1\rho_1 U_y^1, \alpha_2\rho_2 U_x^2, \alpha_2\rho_2 U_y^2\right) \tag{10}$$

and a scalar function

$$\eta(W) = \frac{1}{2}\left(\sum_{i=1,2} \alpha_i\rho_i U^i U^i \right) + \alpha_2 H_2(\alpha_2) + \alpha_1\rho_1 H_1(\rho_1) \tag{11}$$

with

$$\alpha_2^2 H_2'(\alpha_2) = \Xi(\alpha_2) \tag{12a}$$

$$\rho_1^2 H_1'(\rho_1) = P_1(\rho_1) \tag{12b}$$

and the following flux:

$$f_\eta^{\text{nv}}(W) = \frac{1}{2}\left(\sum_{i=1,2} \left\{\alpha_i\rho_i \|U^i\|^2 U^i\right\} \right) + P_1(\rho_1)\left(\sum_{i=1,2} \left\{\alpha_i U^i\right\} \right)$$
$$+ \{\alpha_2 H_2(\alpha_2) + \Xi(\alpha_2)\}U^2 + \alpha_1\rho_1 H_1(\rho_1) U^1 \tag{13}$$

Using these definitions and focusing on adequately regular solutions of Eqs. (1–4), we get a result that is close to the one given in previous work.[16]

Proposition 1: We assume that W represents a regular solution of the set (1–4). Then, there exists a flux $f_\eta^v(W, \nabla W)$ such that

$$[\eta(W)]_{,t} + \nabla \cdot \left[f_\eta^{\text{nv}}(W)\right] + \nabla \cdot \left[f_\eta^v(W, \nabla W)\right] = S_\eta(W, \nabla W)$$

with $S_\eta(W, \nabla W) \le 0$. The source term is

$$S_\eta(W, \nabla W) = (U_1 - U_2) \cdot I_1 + \alpha_1 \sum_1^{\text{visc}} \frac{(\nabla U^1 + \nabla^t U^1)}{2}$$
$$+ \alpha_2 \sum_2^{\text{visc}} \frac{(\nabla U^2 + \nabla^t U^2)}{2}$$

Hereinafter, $[\phi]$ is the jump of ϕ through some discontinuity traveling at speed σ, whatever ϕ stands for. Thus, in the pure nonviscous limit case, the latter provides

$$-\sigma[\eta(W)] + \left[f_\eta^{\text{nv}}(W)\right] \le 0 \tag{14}$$

The latter entropy inequality cannot be rewritten in a simple way, as it can within the framework of gasdynamics, for instance.[17] However, it actually enables the control of the suitability of the computed solutions as outlined in some cases described in Ref. 15 that involve four shock waves or in the computational examples to be detailed subsequently.

Another point, which is well known now, is that the convective system involved in system (1–4), which has no conservative form, represents a conditionally hyperbolic system. Hence, two distinct celerities are defined to examine the hyperbolicity domain:

$$c_2^2 = (\rho_2)^{-1}\left[\frac{\mathrm{d}\Xi(\alpha_2)}{\mathrm{d}\alpha_2}\right] \tag{15}$$

$$c_1^2 = \frac{\mathrm{d}P_1(\rho_1)}{\mathrm{d}\rho_1} \tag{16}$$

We introduce the relative velocity $U^r = U^2 - U^1$, and thus, we may rewrite the convective system as

$$W_{,t} + A_x W_{,x} + A_y W_{,y} = 0 \tag{17}$$

Straightforward analytic expressions of the eigenvalues of the matrix $(n_x A_x + n_y A_y)$ cannot be derived. This obviously implies that the Riemann problem cannot be investigated when considering arbitrary initial data. Expansions (of eigenvalues) in terms of the relative velocity U^r (or the volumetric fraction α_2) may be performed, as pointed out previously by other authors[1,3,5]; thus, for small enough values of the parameter $\|U^r\|/c_1$ (or α_2), approximate Riemann solvers may be constructed to compute flows in which the normalized relative velocity (or α_2) remains uniformly bounded. These assumptions are not considered herein. Thus, the suitability of computational results will be checked using sufficient conditions to ensure hyperbolicity:

$$1 > 2\|U^r\|/c_1 \tag{18}$$

$$1 > 4\left(c_2^2/c_1^2 + \alpha_2\rho_1/\alpha_1\rho_2\right) \tag{19}$$

$$\left(1 - \|U^r\|^2/c_1^2\right)\left(\alpha_1\rho_2 c_2^2/\alpha_2\rho_1 c_1^2 + 1\right) > 1 \tag{20}$$

Conditions (18–20) are not realizability conditions, as occurs, for example, when investigating single-phase turbulent flows.[18] We also emphasize that adequately regular (at least C^1) solutions of the set (1–4) only fulfill

$$0 \le \alpha_2 \tag{21a}$$

$$0 \le \alpha_1\rho_1 \tag{21b}$$

IV. Finite Volume Algorithm to Compute the Four-Equation Model

The following finite volume scheme allows computing time-dependent flows on unstructured meshes. The primal mesh is generated using a regular triangulation of the computational domain. The cell-vertex finite volume mesh is then based on $P1$ nodes. Viscous terms on the right-hand sides of Eqs. (3) and (4) are accounted for using a standard $P1$ finite element Galerkin formulation.

A. Fractional Step Technique

We first detail the implementation of convective terms. Because we cannot obtain an approximate Riemann solver to get a stable scheme in a straightforward manner (using Roe's linearized Riemann solver, for instance), we apply a fractional step technique to compute the convective subset. This approach has been extensively investigated before within the Euler framework,[19,20] using Roe's Riemann solver to compute each step, and has proven to give a similar rate of convergence when computing basic Riemann problems including shock waves and rarefaction waves. Hence, we first solve

$$(\alpha_1\rho_1)_{,t} = 0 \tag{22}$$

$$(\alpha_2)_{,t} + \nabla \cdot \left(\alpha_2 \boldsymbol{U}^2\right) = 0 \tag{23}$$

$$\left(\alpha_1\rho_1\boldsymbol{U}^1\right)_{,t} + \nabla \cdot \left(\alpha_1\rho_1 \boldsymbol{U}^1 \otimes U^1\right) = 0 \tag{24}$$

$$\left(\alpha_2\rho_2\boldsymbol{U}^2\right)_{,t} + \nabla\cdot\left(\alpha_2\rho_2\boldsymbol{U}^2\otimes\boldsymbol{U}^2\right) + \nabla\Xi(\alpha_2) = 0 \tag{25}$$

and then solve

$$(\alpha_1\rho_1)_{,t} + \nabla\cdot\left(\alpha_1\rho_1\boldsymbol{U}^1\right) = 0 \tag{26}$$

$$(\alpha_2)_{,t} = 0 \tag{27}$$

$$\left(\alpha_1\rho_1\boldsymbol{U}^1\right)_{,t} + \alpha_1\nabla P_1(\rho_1) = 0 \tag{28}$$

$$\left(\alpha_2\rho_2\boldsymbol{U}^2\right)_{,t} + \alpha_2\nabla P_1(\rho_1) = 0 \tag{29}$$

The system of Eqs. (22–25) is a hyperbolic system in conservative form, and that of Eqs. (26–29) is a nonconservative hyperbolic system. More precisely, if we introduce some normal vector $\boldsymbol{n}$, rewrite these equations in the new frame $(\boldsymbol{n}, \iota)$, and examine one-dimensional Riemann problems in the $\boldsymbol{n}$ direction, the following holds:

Proposition 2: If we define

$$X(\alpha_2) = \int_0^{\alpha_2} \frac{(\Xi'(\alpha)/\rho_2)^{\frac{1}{2}}}{\alpha}\,\mathrm{d}\alpha$$

the one-dimensional Riemann problem associated with Eqs. (22–25) and initial data (W_L, W_R) has a unique solution with positive mass fractions if and only if

$$\left(\boldsymbol{U}_R^2 - \boldsymbol{U}_L^2\right)\cdot\boldsymbol{n} < (X_2)_L + (X_2)_R$$

Furthermore, the maximum principle for the volumetric fraction is preserved through this step.

The proof[15] actually shows that the specific unbounded form of the function $g(\alpha_2)$ in Eq. (7) is compulsory to prevent occurrence of negative values of $(1-\alpha_2)$. This is also in agreement with theoretical results detailed in Ref. 13. We emphasize that the model introduced by many authors to compute dilute flows[4] does not preserve the maximum principle. Up to now, this important feature has never been pointed out in the literature.

Proposition 3: For some given function f, we set $\bar{f} = (f_L + f_R)/2$ but also $[f] = f_R - f_L$, where L and R subscripts refer to the left-hand side and the right-hand side of a discontinuity traveling at speed σ. We introduce approximate jump conditions[2,10–12]

$$\sigma[\alpha_1\rho_1] = \left[\alpha_1\rho_1\boldsymbol{U}^1\cdot\boldsymbol{n}\right], \qquad \sigma[\alpha_2] = 0$$

$$\sigma\left[\alpha_1\rho_1\boldsymbol{U}^1\cdot\boldsymbol{n}\right] = \overline{\alpha_1}[P_1(\rho_1)], \qquad \sigma\left[\alpha_2\rho_2\boldsymbol{U}^2\cdot\boldsymbol{n}\right] = \overline{\alpha_2}[P_1(\rho_1)]$$

where σ is the speed of the discontinuity. Then, the one-dimensional Riemann problem associated with the nonconservative system [Eqs. (26–29)], preceding jump conditions, and initial data (W_L, W_R) has a unique solution with positive mass fractions if and only if

$$\left[\left(\alpha_1\rho_1\boldsymbol{U}^1\right)_R - \left(\alpha_1\rho_1\boldsymbol{U}^1\right)_L\right]\cdot\boldsymbol{n} < 2\frac{(\alpha_1\rho_1c_1)_L + (\alpha_1\rho_1c_1)_R}{(\gamma+1)}$$

The maximum principle for the volumetric fraction α_2 is still preserved.

B. Approximate Riemann Solvers

To compute the system of Eqs. (22) and (24), which uncouples from Eqs. (23) and (25), we use a Godunov solver rather than a Roe-type solver because this can be easily done and generates no increase of the computational effort. Note that, when the mass fraction (α_1, ρ_1) is uniform over all of the computational domain, Eq. (24) identifies with Burger's equation. Subset (23) and (25) is a conservative system, which is the straight counterpart of isentropic Euler equations, though it includes a rather unusual form of the pressure. Hence, a standard Roe's scheme[21] is implemented to compute Eqs. (23) and (25), the details of which are not recalled here. Hereinafter, Δt is the time step at time t^n, Γ_i is the boundary of the finite volume Ω_i. Also $\boldsymbol{W}_i^n$ is the mean value of the conservative variable $\boldsymbol{W}$ over cell i at time t^n, and $\boldsymbol{n}_{ij}$ is the outward normal unit vector on interface ij between two cells indexed by i and j. Γ_{ij} is the contact surface between cells i and j, and $V(i)$ are neighboring cells of cell i. The control volumes that have been used in computations to be presented is shown in Fig. 1. This requires constructing, first, a triangulation of the computational domain; afterwards, a dual mesh centered on $P1$ nodes is generated. Thus, the whole may be written as

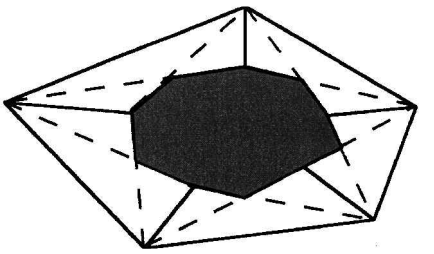

Fig. 1 Control volume.

$$\mathrm{vol}(\Omega_i)\left(\boldsymbol{W}_i^* - \boldsymbol{W}_i^n\right) + \Delta t\sum_{j\in V(i)}\boldsymbol{G}^{\mathrm{num}}\left(\boldsymbol{W}_i^n, \boldsymbol{W}_j^n, \boldsymbol{n}_{ij}\right)\Gamma_{ij} = 0 \tag{30a}$$

with

$$\boldsymbol{G}^{\mathrm{num}}\left(\boldsymbol{W}_i^n, \boldsymbol{W}_j^n, n_{ij}\right) = \begin{pmatrix} 0 \\ \left\{\alpha_2\boldsymbol{U}^2\cdot\boldsymbol{n}\right\}_{ij}^{\mathrm{Roe}} \\ \left\{\left(\alpha_1\rho_1\boldsymbol{U}^1\cdot\boldsymbol{n}\right)\boldsymbol{U}^1\right\}_{ij}^{\mathrm{Godunov}} \\ \left\{\left(\alpha_2\rho_2\boldsymbol{U}^2\cdot\boldsymbol{n}\right)\boldsymbol{U}^2 + \Xi\boldsymbol{n}\right\}_{ij}^{\mathrm{Roe}} \end{pmatrix} \tag{30b}$$

where superscript Roe refers to standard Roe's scheme for isentropic gasdynamics. The remaining part of the flux is defined as follows:

$$\text{If} \quad \left(\alpha_1\rho_1\boldsymbol{U}^1\cdot\boldsymbol{n}\right)_i^n \le 0 \quad \text{and} \quad \left(\alpha_1\rho_1\boldsymbol{U}^1\cdot\boldsymbol{n}\right)_j^n \ge 0$$

$$\left\{\left(\alpha\rho_1\boldsymbol{U}^1\cdot\boldsymbol{n}\right)\boldsymbol{U}^1\right\}_{ij}^{\mathrm{Godunov}} = 0$$

otherwise

$$\left\{\left(\alpha\rho_1\boldsymbol{U}^1\cdot\boldsymbol{n}\right)\boldsymbol{U}^1\right\}_{ij}^{\mathrm{Godunov}} = \left(\alpha_1\rho_1\boldsymbol{U}^1\cdot\boldsymbol{n}\right)_i^n \quad \text{if} \quad \left(\hat{\boldsymbol{U}}^1\cdot\boldsymbol{n}\right)ij \ge 0$$

$$\left\{\left(\alpha\rho_1\boldsymbol{U}^1\cdot\boldsymbol{n}\right)\boldsymbol{U}^1\right\}_{ij}^{\mathrm{Godunov}} = \left(\alpha_1\rho_1\boldsymbol{U}^1\cdot\boldsymbol{n}\right)_j^n \quad \text{if} \quad \left(\hat{\boldsymbol{U}}^1\cdot\boldsymbol{n}\right)ij \le 0 \tag{30c}$$

where

$$\left(\hat{\boldsymbol{U}}^1\cdot\boldsymbol{n}\right)_{ij} = \frac{\left\{(\alpha_1\rho_1)_i^n\right\}^{\frac{1}{2}}(\boldsymbol{U}^1\cdot\boldsymbol{n})_i^n + \left\{(\alpha_1\rho_1)_j^n\right\}^{\frac{1}{2}}(\boldsymbol{U}^1\cdot\boldsymbol{n})_j^n}{\left\{(\alpha_1\rho_1)_i^n\right\}^{\frac{1}{2}} + \left\{(\alpha_1\rho_1)_j^n\right\}^{\frac{1}{2}}} \tag{30d}$$

Computation of the second step involving Eqs. (26–29) is more difficult because it contains some nonconservative terms. Two different schemes have been derived to cope with this subset. We only describe the first scheme. This kind of scheme was introduced previously[22–24] to compute turbulent compressible flows using one- or two-equation models. It is based on a straightforward integration of the nonconservative set (26–29) on the two-dimensional control volume Ω_i; thus,

$$\mathrm{vol}(\Omega_i)\left(\boldsymbol{W}_i^{**} - \boldsymbol{W}_i^*\right) + \Delta t\sum_{j\in V(i)}\boldsymbol{F}^{\mathrm{Roe}}\left(\boldsymbol{W}_i^*, \boldsymbol{W}_j^*, \boldsymbol{n}_{ij}\right)\Gamma_{ij} + \Delta t\boldsymbol{S}_i(\boldsymbol{W}^*) = 0 \tag{31a}$$

setting

$$\boldsymbol{S}_i^t(\boldsymbol{W}^*) = \left(0, 0(\alpha_1)_i^*\sum_{j\in V(i)}\left\{\overline{\boldsymbol{P}(\rho_1^*)}\right\}_{ij}\boldsymbol{n}_{ij}\Gamma_{ij}, \right.$$

$$\left.(\alpha_2)_i^*\sum_{j\in V(i)}\left\{\overline{\boldsymbol{P}(\rho_1^*)}\right\}_{ij}\boldsymbol{n}_{ij}\Gamma_{ij}, \right) \tag{31b}$$

In formula (31b), a centered scheme is used, which means that $\{\overline{\boldsymbol{P}(\rho_1^*)}\}_{ij} = ([\boldsymbol{P}(\rho_1^*)]_i + [\boldsymbol{P}(\rho_1^*)]_j)/2$. The Roe-type numerical flux

in Eq. (31a) is chosen to be in agreement with approximate jump conditions detailed in Proposition 3. The numerical flux is defined as follows:

$$\boldsymbol{F}_{ij}^{\mathrm{Roe}}\left(\boldsymbol{W}_i^*, \boldsymbol{W}_j^*, \boldsymbol{n}_{ij}\right) = \left[\boldsymbol{F}\left(\boldsymbol{W}_i^*, \boldsymbol{n}_{ij}\right) + \boldsymbol{F}\left(\boldsymbol{W}_j^*, \boldsymbol{n}_{ij}\right)\right]/2 - \left|\boldsymbol{B}\left(\boldsymbol{W}_i^*, \boldsymbol{W}_j^*, \boldsymbol{n}_{ij}\right)\right|\left(\boldsymbol{W}_j^* - \boldsymbol{W}_i^*\right)/2 \tag{32}$$

where the continuous flux $\boldsymbol{F}(\boldsymbol{W}, \boldsymbol{n})$ is defined as

$$\boldsymbol{F}^t(\boldsymbol{W}, \boldsymbol{n}) = \left(\alpha_1\rho_1\boldsymbol{U}^1 \cdot \boldsymbol{n}, 0, 0, 0, 0, 0\right) \tag{33}$$

The matrix $\boldsymbol{B}(\boldsymbol{W}_i, \boldsymbol{W}_j, \boldsymbol{n}_{ij})$ satisfies

$$\boldsymbol{F}(\boldsymbol{W}_j, \boldsymbol{n}_{ij}) - \boldsymbol{F}(\boldsymbol{W}_i, \boldsymbol{n}_{ij}) + \boldsymbol{X}_{ij} = \boldsymbol{B}(\boldsymbol{W}_j, \boldsymbol{W}_i, \boldsymbol{n}_{ij})(\boldsymbol{W}_j - \boldsymbol{W}_i) \tag{34}$$

where the contribution $\boldsymbol{X}_{ij}$ accounts for the nonconservative terms present in Eqs. (28) and (29):

$$\boldsymbol{X}_{ij} = \begin{pmatrix} 0 \\ 0 \\ \dfrac{(\alpha_1)_i + (\alpha_1)_j}{2}([P_1(\rho_1)_j] - [P_1(\rho_1)_i])\boldsymbol{n}_{ij} \\ \dfrac{(\alpha_2)_i + (\alpha_2)_j}{2}([P_1(\rho_1)_j] - [P_1(\rho_1)_i])\boldsymbol{n}_{ij} \end{pmatrix} \tag{35}$$

This formulation obviously identifies with the original Roe's scheme when restricted to the framework of systems of conservation laws.

C. Implementation of Source Terms

Once convective effects have been accounted for, drag forces are implemented in a very simple way. Given some ** values of the conservative variable $\boldsymbol{W}$, compute

$$(\alpha_1\rho_1)_i^{n+1} = (\alpha_1\rho_1)_i^{**}, \qquad (\alpha_2)_i^{n+1} = (\alpha_2)_i^{**} \tag{36}$$

$$\begin{bmatrix} \left(\alpha_1\rho_1U^1\right)_i^{n+1} \\ \left(\alpha_2\rho_2U^2\right)_i^{n+1} \end{bmatrix} = \begin{bmatrix} \left(\alpha_1\rho_1U^1\right)_i^{**} \\ \left(\alpha_2\rho_2U^2\right)_i^{**} \end{bmatrix} + \Delta t(\alpha_1\rho_1)_i^{n+1}(\alpha_2)_i^{n+1}(K)_i^{**}\begin{bmatrix} (U^2)_i^{n+1} - (U^1)_i^{n+1} \\ (U^1)_i^{n+1} - (U^2)_i^{n+1} \end{bmatrix} \tag{37}$$

Other ways to deal with source terms have been recently proposed.[25]

V. Numerical Results

A. Shock-Tube Test Case Without Drag Effects

We begin with the computation of the nonconservative convective system associated with Eqs. (1–4), which means that both viscous and drag effects are neglected ($\mu_1 = \mu_2 = K = 0$). Computational results subsequently shown were obtained using the already mentioned first-order approximate Riemann solver, on a one-dimensional regular mesh with 1500 nodes. Physical values are $(q_2^2)_0 = \frac{15}{2}\ \mathrm{m^2\ s^{-2}}$, $\rho_2 = 1000\ \mathrm{kg\ m^{-3}}$, $\alpha_{\max} = 0.64$, and $e_c = 1$. The test case is a shock-tube problem, with the following initial data (Figs. 2a–2d):

$$W(x < 0, t = 0) = \begin{pmatrix} \alpha_1\rho_1 = 0.5 \\ \alpha_2 = 0.5 \\ \alpha_1\rho_1U^1 = 0 \\ \alpha_2\rho_2U^2 = 0 \end{pmatrix}$$

$$W(x > 0, t = 0) = \begin{pmatrix} \alpha_1\rho_1 = 0.12 \\ \alpha_2 = 0.6 \\ \alpha_1\rho_1U^1 = 0 \\ \alpha_2\rho_2U^2 = 0 \end{pmatrix}$$

Both the 2-wave and 4-wave are shocks, whereas the 1-field and 3-field are rarefaction waves. Because of the initial high void fractions on each side of the initial membrane, as well as the high density of particles, both the velocity and void fraction of the particle phase seem to ignore the presence of the rarefaction wave and the shock wave within the gas phase. On the contrary, profiles of the mean gas density and mean velocity field are greatly modified by the presence of particles, compared with what occurs when the void fraction is set to zero. It must be emphasized that when the turbulent kinetic energy is much smaller, the 2- and 3-waves can hardly be distinguished.

B. Computation of a Gas–Solid Two-Phase Flow in a Simple Nozzle

Figure 3 is devoted to the computation of the four-equation model in a nozzle. We now account for drag effects and set $\gamma = \frac{7}{5}$, $(q_2^2)_0 = \frac{15}{2}\ \mathrm{m^2\ s^{-2}}$, $\rho_2 = 2500\ \mathrm{kg\ m^{-3}}$, $\alpha_{\max} = 0.64$, and $e_c = 1$. The particle diameter, which is used to compute the drag coefficient K, equals 100 μm. The mesh in this case contains around 8500 $P1$ nodes. A zoom on the mesh in the convergent part of the nozzle

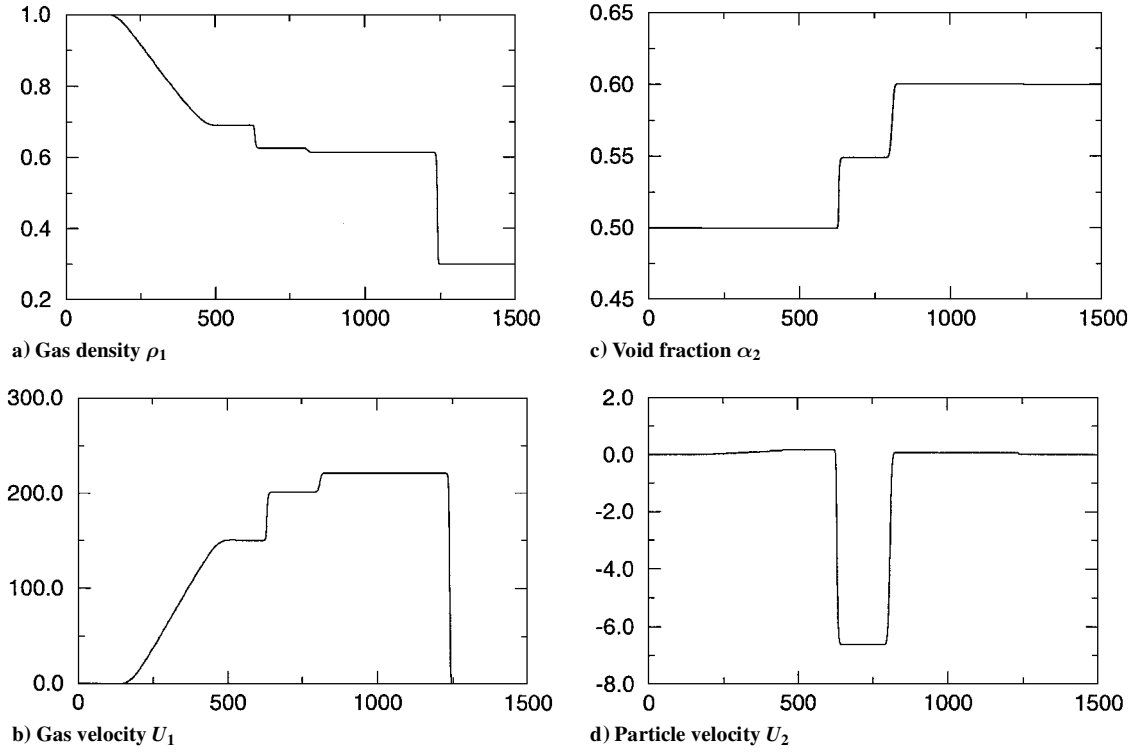

Fig. 2 Shock tube test case without drag effects.

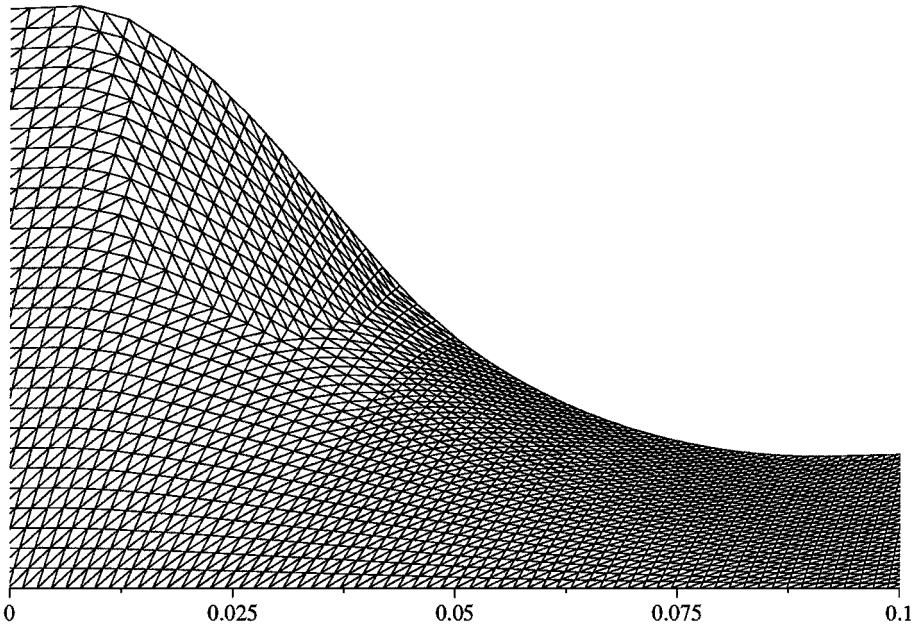

a) Unstructured mesh for the convergent part of the nozzle

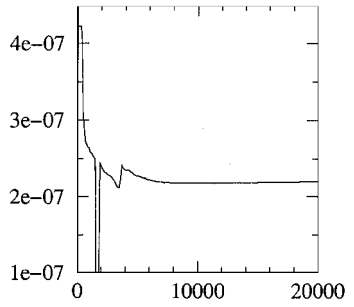

b) Evolution of the time step vs time iterations

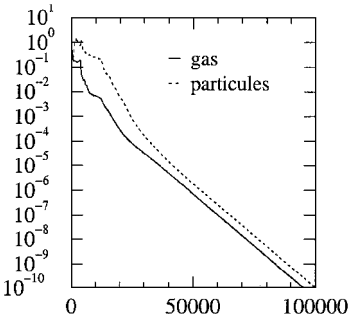

c) Evolution of the mass residuals for both the gas and solid phases

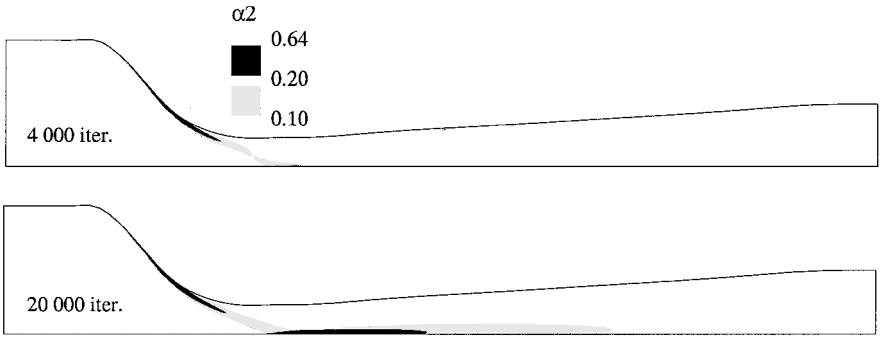

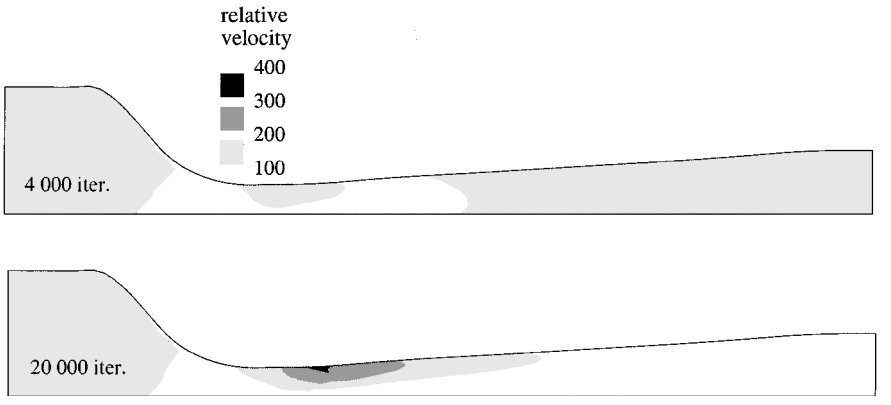

d) Transient solution

Fig. 3 Computation of a gas–solid two-phase flow in a simple nozzle.

is shown in Fig. 3a. The volumetric fraction is 0.01 (respectively, 10^{-6}) in the inlet channel (respectively, downstream); inlet gas and particle velocities are assumed to be equal to 200 m/s. The ratio of mean gas pressures between inlet and outlet is 1.1427. Viscous effects have been neglected in this computation. The evolution of the time stepping is shown in Fig. 3b. Getting the mass residuals (Fig. 3c) lower than 10^{-5} and 10^{-4} for the gas phase and the particle phase, respectively, requires around 20,000 time steps, when using the explicit scheme. The mass residual for phase k is computed at time $n\Delta t$ as follows:

$$R_k^n = \frac{\left\| (\alpha_k \rho_k)^{n+1} - (\alpha_k \rho_k)^n \right\|_{L^2}}{\left\| (\alpha_k \rho_k)^n \right\|_{L^2}}$$

The distribution of particles in the nozzle greatly influences the mean gas flow. From top to bottom (Fig. 3d), we can examine the transient solution, focusing on the volumetric fraction of particles α_2 and then on the relative velocity, which is still very large around the steady state (the maximum value of $\|U^r\|/c_1$ is about 1). Particles aggregate on the near-wall region in the convergent part of the nozzle and also on the symmetry axis, just before enlargement. Sudden decrease of the time step in Fig. 3b is due to the occurrence of a cluster in the near-wall region of the convergent part of the nozzle. Details on the implementation of the wall boundary conditions can be found in the Appendix. These must be obviously accounted for in a physical way to prevent the occurrence of negative values of the expected positive mass fractions.

C. Shock-Tube Test Case with Drag Effects

We still neglect viscous effects and account for drag effects. We set $\gamma = \frac{7}{5}$, $(q_2^2)_0 = \frac{15}{2}$ m^2 s^{-2}, $\rho_2 = 2500$ kg m^{-3}, $\alpha_{\max} = 0.64$, and $e_c = 1$. The particle diameter still is 100 μm. The computation is performed on an unstructured two-dimensional mesh with 10,000 nodes (representing approximately 1000 cells in the x direction). The initial data are exactly the same as in the first test case. Variables α_2 and ρ_1 are shown in Fig. 4 (circles are used to plot results obtained using the four-equation model). The behavior of the mean density is obviously completely different (see Fig. 2a for comparison). The relative velocity is very small now, compared with the first test case.

We may compare results obtained using the present four-equation model and those obtained using a three-equation mode,[13] where the granular pressure is still taken into account but the relative velocity is set to zero. More precisely, the three-equation model reads

$$(\alpha_1\rho_1)_{,t} + \nabla\cdot(\alpha_1\rho_1 U) = 0, \qquad (\alpha_2)_{,t} + \nabla\cdot(\alpha_2 U) = 0$$

$$[(\alpha_1\rho_1 + \alpha_2\rho_2)U]_{,t} + \nabla\cdot[(\alpha_1\rho_1 + \alpha_2\rho_2)U\otimes U]$$

$$+ \nabla[P_1(\rho_1) + \Xi(\alpha_2)] - (\alpha_1\rho_1 + \alpha_2\rho_2)g = 0$$

and the scheme used to compute this conservative system is based on the original idea of Gallouet and Masella.[26] A straight line is used to plot results obtained with the three-equation model in Fig. 4. The notation P_{tot}, which is used in Fig. 4, is

$$P_{\text{tot}} = P_1(\rho_1) + \Xi(\alpha_2)$$

This quantity should remain constant through the contact discontinuity of the three-equation model, which is perfectly satisfied by the computation. It should increase in the 1-shock and also in the 3-rarefaction wave of the three-equation model. Also, the ratio of mass fractions $(\alpha_2\rho_2/\alpha_1\rho_1)$ should not vary in both the 1-wave and the 3-wave; this is also very well predicted by the scheme. Note that computational results provided by these two a priori different models are very similar. The comparison of both calculations even shows better agreement when the particle diameter goes to zero; this is because, when drag effects increase, the time required to reach null relative velocities gets smaller and smaller.

D. Schematic Behavior of the Scheme Near-Wall Boundaries

This test case (Fig. 5) involves four shock waves. This one is based on the following initial data:

$$W(x<0,t=0) = \begin{pmatrix} \alpha_1\rho_1 = 0.5 \\ \alpha_2 = 0.5 \\ \alpha_1\rho_1 U^1 = 350 \\ \alpha_1\rho_1 V^1 = 0 \\ \alpha_2\rho_2 U^2 = 6250 \\ \alpha_2\rho_2 V^2 = 0 \end{pmatrix}$$

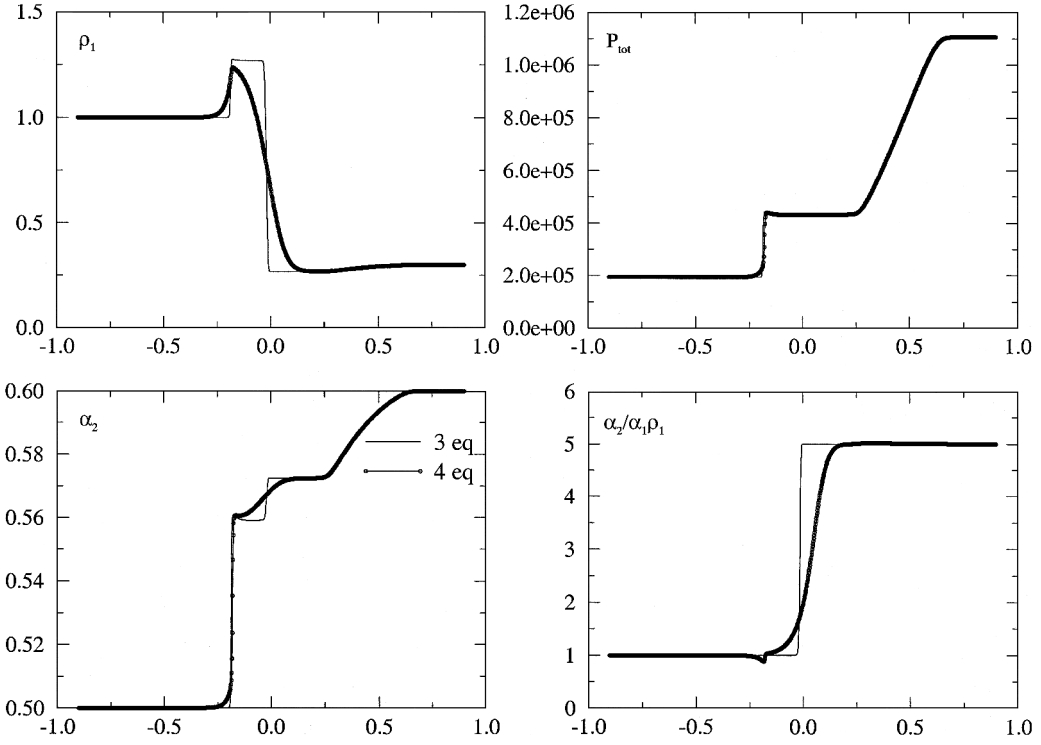

Fig. 4 Shock-tube test case with drag effects.

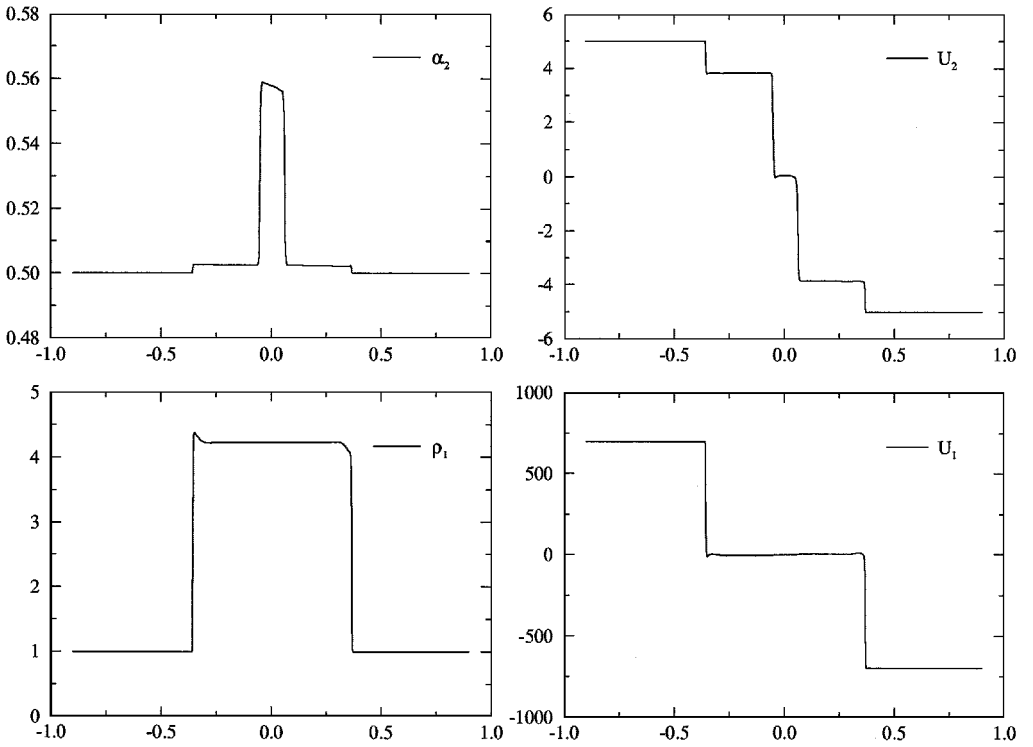

Fig. 5 Schematic behavior of the scheme near wall boundaries.

$$W(x>0,t=0)=\begin{pmatrix}\alpha_1\rho_1=0.5\\ \alpha_2=0.5\\ \alpha_1\rho_1U^1=-350\\ \alpha_1\rho_1V^1=0\\ \alpha_2\rho_2U^2=-6250\\ \alpha_2\rho_2V^2=0\end{pmatrix}$$

A two-dimensional mesh is used. A rectangular domain is divided in rectangles first; these are then divided along each diagonal. The mesh contains 1000 nodes in the x direction. Thus, the numerical solution cannot be a pure one-dimensional solution (both cross velocity components V^1 and V^2 evolve in time), which is confirmed by the presence of small losses of monotonicity in the vicinity of shock waves. Physical constants are the same as in the first test case, except for the particle density $\rho_2=2500$ kg m^{-3}. This numerical experiment with symmetrical initial data has two main advantages. First, it enables the examination of the capability of the scheme to preserve the maximum principle for the void fraction because the kinetic energy is converted into pressure within each phase in the central region, which results in an increase of the void fraction. Second is that this schematic case enables simulating an impinging jet on a wall boundary, when one applies for the mirror state technique, which is shown in the Appendix.

E. Computation of Dense Fluidized Beds

We now examine the case of a rectangular box (where $L_{\text{bed}}=\frac{1}{2}$ m long and $H=1\frac{1}{2}$ m high) containing a bed of particles. The lower part of the box is a grid that prevents particles from going out but allows an inlet upwards going gas flow. Left- and right-hand-side boundaries are rigid walls, and the upper part is open. The initial conditions for the gas density and the mean volumetric fraction of particles are, for $x, y<0.476$, $t=0$,

$$\begin{pmatrix}\rho_1=1\\ \alpha_2=0.63\end{pmatrix}$$

and, for $x, y>0.476$, $t=0$,

$$\begin{pmatrix}\rho_1=1\\ \alpha_2=0.000001\end{pmatrix}$$

Both gas and particles are at rest at the beginning of the computation. Then, a constant and uniform inlet gas flow is imposed under the grid, and the mean inlet gas velocity and the mean density of the gas are

$$\begin{pmatrix}U_1=0\\ V_1=0.8\\ \rho_1=1\end{pmatrix}$$

We still set $\gamma=\frac{7}{5}$, but the value of the constant $[(q_2^2)_0=0.00015\,\text{m}^2\,\text{s}^{-2}]$ is much smaller than in the earlier computations because of the order of magnitude of the mean particles and gas velocities. The density of particles still is $\rho_2=2500\,\text{kg m}^{-3}$, and the maximum compactness rate and elasticity coefficient are $\alpha_{\max}=0.64$ and $e_c=1$. The particle diameter is equal to 500 μm. The unstructured two-dimensional mesh is based on a primal mesh containing approximately 9400 triangles (Fig. 6a). The mesh is much refined in the lower part of the computational domain, just above the grid. The mean height of the bed $H(t)$ and the mean volumetric fraction of the particle phase $\alpha_{\text{mean}}(t)$, which are plotted in Figs. 6b and 6c, are defined as

$$H(t)=2\left[\int_{x=0}^{x=L\,\text{bed}}\int_{y=0}^{y=H}\alpha_2(x,y,t)y\,dx\,dy\Big/\int_{x=0}^{x=L\,\text{bed}}\int_{y=0}^{y=H}\alpha_2(x,y,t)\,dx\,dy\right]$$

$$\alpha_{\text{mean}}(t)=\int_{x=0}^{x=L\,\text{bed}}\int_{y=0}^{y=H}\alpha_2(x,y,t)\,dx\,dy\Big/H(t)L_{\text{bed}}$$

The normalized bed height is $H(t)/H(0)$. The whole computation lasts 10 s and is highly time dependent. Bubbles are generated either just above the grid or in the bed itself. These may either collapse or grow up to the bed surface. The mean volumetric fraction inside bubbles may go down lower than 5% (Fig. 6d). The maximum principle for the mean volumetric fraction is not violated during this transient computation, though very high values occur, because the maximum value of α_2 is close to 0.6391. From time to time, inside

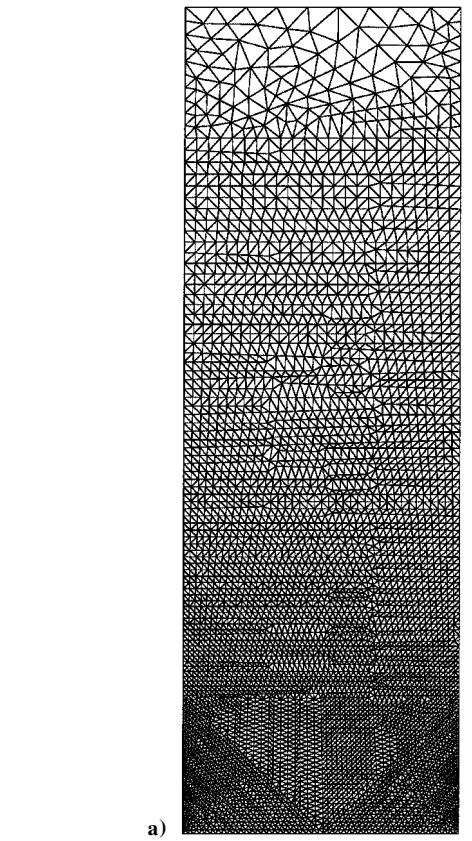

a)

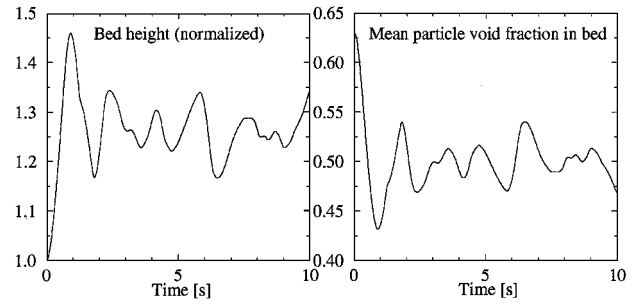

b) c)

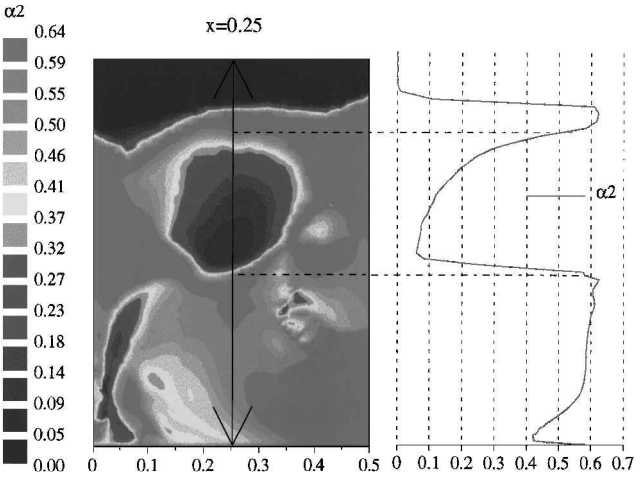

d)

Fig. 6 Computation of dense fluidized beds: a) unstructured mesh used in the box, b) evolution of the normalized bed height vs time, c) evolution of the mean particle void fraction in the bed vs time, and d) particle void fraction distribution in the bed.

some bubbles, the flow no longer is hyperbolic. The influence of the mesh size and of the value of $(q_2^2)_0$ is discussed in Refs. 8 and 13. Other numerical experiments can be found in Ref. 13.

VI. Conclusion

The presented finite volume time-dependent algorithm enables the computation of a four-equation compressible two-fluid model on unstructured meshes. It can be very easily implemented in finite volume codes, using any kind of unstructured mesh. Numerical experiments on unstructured meshes confirm that the scheme behaves well. In particular, it must be emphasized that no violation of the maximum principle was noted [though we use Roe's scheme to compute Eqs. (23) and (25)], even when the initial data are close to the maximum value of the volumetric fraction; this, however, requires specific treatment on the boundary conditions, especially in the wall region. Actually, the theoretical investigation of the one-dimensional Riemann problems provides useful tools for that purpose. More accurate predictions of the particle phase on coarse meshes require, of course, second-order MUSCL-type extension of the basic first-order scheme that is used to predict Eqs. (23) and (25). Implicit discretization of fast (mean gas pressure) waves present in Eqs. (26–29) can be easily achieved. This algorithm is currently used to predict dense fluidized beds. It is also used to predict the propagation of strong gas shock waves entering a dense granular medium. An extension of this scheme enables solving a five-equation two-fluid model, which in addition contains the governing equation of the granular pressure.

Appendix: Numerical Treatment of Wall Boundary Conditions

The whole is based on the use of the mirror state technique. To simplify the presentation, the method is presented in a pure one-dimensional framework. Hence, we focus on the following system issuing from Eqs. (23) and (25):

$$(\alpha_2)_{,t} + \left(\alpha_2 U^2\right)_{,x} = 0 \tag{A1a}$$

$$\left(\alpha_2 \rho_2 U^2\right)_{,t} + \left(\alpha_2 \rho_2 U^2 U^2\right)_{,x} + [\Xi(\alpha_2)]_{,x} = 0 \tag{A1b}$$

We assume that the wall boundary stands on the right side of cell i. If index i refers to the neighboring cell close to the wall boundary, where the average value at time t^n is $(\alpha_2, \alpha_2\rho_2 U^2)_i$, then the mirror state equals $(\alpha_2, -\alpha_2\rho_2 U^2)_i$. The numerical wall flux $\boldsymbol{G}^{\text{num}}$ is then evaluated using these two states and some suitable flux formula. The resulting formula is

$$\boldsymbol{G}^{\text{num}} = (0, \hat{\Xi}) \tag{A2}$$

Actually, one has to distinguish three different cases.

1) If $(U^2)_i > 0$ [which corresponds to a locally impinging flow, and thus to a symmetrical double shock wave in the solution of the one-dimensional Riemann problem associated with Eqs. (A1a) and (A1b)], then

$$\hat{\Xi} = \Xi[(\alpha_2)_i] + \rho_2(\alpha_2)_i (U_2)_i [c_2(\alpha_2)_i + (U_2)_i] \tag{A3}$$

where c_2 is introduced in Eq. (15).

2) If $(U^2)_i < 0$, but complies with

$$\int_0^{(\alpha_2)i} \frac{[\Xi'(\alpha)/\rho_2]^{\frac{1}{2}}}{\alpha}\, d\alpha + (U^2)_i > 0$$

(which corresponds to a decrease of pressure in the wall region and to a symmetrical double rarefaction wave when solving the Riemann problem), then

$$\hat{\Xi} = \Xi(\hat{\alpha}_2) \tag{A4}$$

The value $\hat{\alpha}_2$ is computed by integrating the Riemann invariant in the 1-wave and, hence, solving

$$\int_0^{(\alpha_2)i} \frac{[\Xi'(\alpha)/\rho_2]^{\frac{1}{2}}}{\alpha}\, d\alpha + (U^2)_i = \int_0^{\hat{\alpha}_2} \frac{[\Xi'(\alpha)/\rho_2]^{\frac{1}{2}}}{\alpha}\, d\alpha \tag{A5}$$

3) If

$$\int_0^{(\alpha_2)i} \frac{[\Xi'(\alpha)/\rho_2]^{\frac{1}{2}}}{\alpha}\,\mathrm{d}\alpha + (U^2)_i < 0$$

a vacuum occurs in the solution because the condition detailed in Proposition 2 is violated. In that case, the granular pressure at the wall is simply zero:

$$\hat{\Xi} = 0 \tag{A6}$$

In all cases, $\hat{\Xi}$ corresponds to an approximate value of the wall granular pressure. In the first case, Roe's flux has been used to construct $\hat{\Xi}$. In the second case, the Godunov scheme was preferred because Roe's flux may then lead to some estimated value that is in complete disagreement with physical requirements inasmuch as one should have in that case $\hat{\Xi} < \Xi((\alpha_2)_i)$ This happens (when applying for Roe's numerical flux) when the local Mach number $[(U_2)_i/c_2(\alpha_2)_i]$ becomes smaller than -1 [see expression (A3) for a quick check]. Hence, note that $\hat{\Xi} > \Xi((\alpha_2)_i)$ in the first case and that $\hat{\Xi} < \Xi((\alpha_2)_i)$ in the second case, which is in agreement with the exact solution of the Riemann problem associated with system (A1a) and (A1b). Extension to a two-dimensional framework is straightforward, using invariance of equations under frame rotation and substituting $(\boldsymbol{U}^2 \cdot \boldsymbol{n})$ into U^2, where $\boldsymbol{n}$ is the outward normal unit vector. Similar techniques have been used to compute wall fluxes involved in Eqs. (26–29).

Acknowledgments

The first author has benefited from financial support from Electricité de France during her stay in Laboratoire National d'Hydraulique. All computational facilities were provided by the Research Branch of Electricité de France. Both authors would like to thank Arnaud Boelle, Jean Fabre, and Olivier Simonin for advice and motivating discussions.

References

[1]Raviart, P. A., and Sainsaulieu, L., "A Non Conservative Hyperbolic System Modelling Spray Dynamics. Part I: Solution of the Riemann Problem," *Mathematical Models and Methods in Applied Sciences*, Vol. 5, 1995, pp. 297–333.

[2]Sainsaulieu, L., "Contribution à la modélisation mathématique et numérique des écoulements diphasiques constitués d'un nuage de particules dans un écoulement de gaz," Thèse d'Habilitation, Univ. of Paris VI, Paris, France, 1995.

[3]Sainsaulieu, L., "Finite-Volume Approximation of Two Phase-Fluid Flows Based on an Approximate Roe-Type Riemann Solver," *Journal of Computational Physics*, Vol. 121, No. 1, 1995, pp. 1–28.

[4]Saurel, R., Forestier, A., Veyret, D., and Loraud, J. C., "A Finite-Volume Scheme for Two-Phase Compressible Flows," *International Journal for Numerical Methods in Fluids*, Vol. 18, No. 9, 1994, pp. 803–819.

[5]Toumi, I., and Kumbaro, A., "An Approximate Linearized Riemann Solver for Two-Fluid Model," *Journal of Computational Physics*, Vol. 124, No. 2, 1996, pp. 286–300.

[6]Lun, C. K. K., and Savage, S. B., "The Effect of an Impact Dependent Coefficient of Restitution on Stresses Developped by Sheared Granular Materials," *Acta Mechanica*, Vol. 63, 1986, pp. 15–44.

[7]Gidaspow, D., *Multiphase Flow and Fluidization*, Academic, New York, 1993.

[8]Balzer, G., and Simonin, O., "Extension of Eulerian Gas–Solid Flow Modelling to Dense Fluidized Bed Prediction," *Proceedings of 5th International Symposium on Refined Flow Modelling and Turbulence Measurements*, Presse Nationale de l'Ecole des Ponts et Chaussées, Paris, France, 1993, pp. 417–424.

[9]Simonin, O., "Second Moment Prediction of Disperse Phase Turbulence in Particle Laden Flows," *Proceedings of the 8th Symposium on Turbulent Shear Flows* (Munich, Germany), 1991.

[10]Colombeau, J. F., *Multiplicaton of Distributions*, Springer–Verlag, Berlin, 1992.

[11]Dal Maso, G., Le Floch, P. G., and Murat, F., "Definition and Weak Stability of Non Conservative Products," *Journal de Mathématiques Pures et Appliquées*, Vol. 74, No. 6, 1995, pp. 483–548.

[12]Le Floch, P., "Entropy Weak Solutions to Non Linear Hyperbolic Systems in Non Conservative Form," *Communications in Partial Differential Equations*, Vol. 13, No. 6, 1988, pp. 669–727.

[13]Combe, L., "Simulation numérique d'écoulements gaz-particules sur maillage non structuré," Ph.D. Thesis, Institut de Mécanique des Fluides de Toulouse, Toulouse, France, Sept. 1997.

[14]Goldshtein, A., Shapiro, M., and Gutfinger, C., "Mechanics of Collisional Motion of Granular Materials, Part 3. Self-Similar Shock Wave Propagation," *Journal of Fluid Mechanics*, Vol. 316, 1996, pp. 29–51.

[15]Combe, L., and Hérard, J. M., "Un schéma Volumes-Finis pour la simulation d'un modèle bi-fluide d'écoulements diphasiques compressibles gaz-solide," *Revue Européenne des Eléments Finis*, Vol. 5, No. 2, 1997, pp. 197–231.

[16]Sainsaulieu, L., "Ondes progressives solutions de systèmes convectifs diffusifs et systèmes hyperboliques non conservatifs," *Comptes Rendus Académie des Sciences de Paris*, Vol. 1-312, 1991, pp. 491–494.

[17]Smoller, J., *Shock Waves and Reaction-Diffusion Equations*, Springer–Verlag, Berlin, 1983, pp. 337–367.

[18]Berthon, C., Coquel, F., Hérard, J. M., and Uhlmann, M., "An Approximate Riemann Solver to Compute Compressible Flows Using Second-Moment Closures," AIAA Paper 97-2069, July 1997.

[19]Buffard, T., and Hérard, J. M., "A Conservative Fractional Step Method to Solve Non-Isentropic Euler Equations," *Computer Methods in Applied Mechanics and Engineering*, Vol. 144, No. 3/4, 1997, pp. 199–225.

[20]Buffard, T., and Hérard, J. M., "A Conservative Spliting Scheme to Solve Euler Equations on Unstructured Meshes," *Comptes Rendus Académie des Sciences Paris*, Vol. 2-316, 1993, pp. 575–582.

[21]Roe, P. L., "Approximate Riemann Solvers, Parameter Vectors and Difference Schemes," *Journal of Computational Physics*, Vol. 43, 1981, pp. 357–372.

[22]Forestier, A., Hérard, J. M., and Louis, X., "A Godunov Type Solver to Compute Turbulent Compressible Flows," *Comptes Rendus Académie des Sciences Paris*, Vol. 1-324, 1997, pp. 919–926.

[23]Hérard, J. M., "An Approximate Riemann Solver to Compute a Non Conservative Hyperbolic System Derived from a Turbulent Compressible Model," Eléctricité de France, Rept. HE-41/95/009/A, Direction Etudes et Recherches, Lab. National d'Hydraulique, Chatou, France, May 1995 (in French).

[24]Hérard, J. M., *Suitable Algorithms to Preserve the Realisability of Reynolds Stress Closures*, Fluids Engineering Div. Vol. 215, American Society of Mechanical Engineers, New York, 1995, pp. 73–80.

[25]Burman, E., and Sainsaulieu, L., "Numerical Analysis of Two Operator Splitting Methods for an Hyperbolic System of Conservation Laws with Stiff Relaxation Terms," *Computer Methods in Applied Mechanics and Engineering*, Vol. 128, No. 3–4, 1995, pp. 291–314.

[26]Gallouet, T., and Masella, J. M., "A Rough Godunov Scheme," *Comptes Rendus Académie des Sciences Paris*, Vol. 1-323, 1996, pp. 77–84.

J. Kallinderis
Associate Editor